



# Hybrid spiral scanning in a double-clad fiber-based handheld confocal scanning light ophthalmoscope

FRANKLIN WEI,<sup>1,2,\*</sup>  KRISTEN HAGAN,<sup>1</sup> CHRISTIAN VIEHLAND,<sup>1</sup> YUANKAI K. TAO,<sup>3</sup> ANTHONY N. KUO,<sup>1,4</sup> JOSEPH A. IZATT,<sup>1,2,4</sup> AND AL-HAFEEZ DHALLA<sup>1,4</sup>

<sup>1</sup>Department of Biomedical Engineering, Duke University, Durham, NC 27708, USA

<sup>2</sup>Department of Electrical and Computer Engineering, Duke University, Durham, NC 27708, USA

<sup>3</sup>Department of Biomedical Engineering, Vanderbilt University, Nashville, TN 37232, USA

<sup>4</sup>Department of Ophthalmology, Duke University Medical Center, Durham, NC 27708, USA

\*[me@franklinwei.com](mailto:me@franklinwei.com)

**Abstract:** High-speed, accessible, and robust *in vivo* imaging of the human retina is critical for screening of retinal pathologies, such as diabetic retinopathy, age-related macular degeneration, and others. Scanning light ophthalmoscopy (SLO) is a retinal imaging modality that produces digital, *en face* images of the human retina with superior image gradability rates when compared to the current standard of care in screening for these diseases, namely the flood-illumination handheld fundus camera (HFC). However, current-generation commercial SLO systems are mostly tabletop devices, limiting their accessibility and utility in screening applications. Moreover, most existing SLO systems use raster scan patterns, which are both inefficient and lead to undesired subject gaze drift when used with visible or pseudo-visible illumination. Non-raster scan patterns, especially spiral scanning as described herein, promise advantages in both scan efficiency and reduced subject eye motion. In this work, we introduce a novel “hybrid spiral” scan pattern and the associated hardware design and real-time image reconstruction techniques necessary for its implementation in an SLO system. Building upon this core hybrid spiral scanning SLO (HSS-SLO) technology, we go on to present a complete handheld HSS-SLO system, featuring a fiber-coupled portable patient interface which leverages a dual-clad fiber (DCF) to form a single-path optical topology, thus ensuring mechanically robust co-alignment of illumination and collection apertures, a necessity for a handheld system. The feasibility of HSS-SLO for handheld, *in vivo* imaging is demonstrated by imaging eight human volunteers.

© 2023 Optica Publishing Group under the terms of the [Optica Open Access Publishing Agreement](#)

## 1. Introduction

Scanning light (or laser) ophthalmoscopy (SLO) is a retinal imaging modality which scans a focused spot of light across the retina in order to construct a two-dimensional *en face* reflectance image [1]. The predominant variant of SLO is confocal SLO (cSLO), wherein a confocal pinhole (often the endface of a multimode optical fiber) is placed in a plane conjugate to an illuminated point on the retina, thus allowing axial sectioning and rejection of corneal glare, analogous to that of a confocal microscope [2]. Mechanically scanning the focused spot across the retina in a dense scan pattern then enables two-dimensional area image reconstruction, which is often accomplished by digital means—except in the very earliest of systems.

cSLO has clinical applications in screening for various ophthalmic pathologies, including diabetic retinopathy, the leading cause of blindness in working age adults [3]. For this and other applications, there is a need for a low-cost, handheld cSLO device, because a portable form factor would offer enhanced screening to patients who are otherwise underserved by current, more limited technologies: tabletop cSLO devices, tabletop fundus cameras, and handheld fundus

cameras (HFCs), which are all either non-portable or suffer from poor image gradability rates [4–8]. However, the design of a portable, handheld cSLO system poses challenges: traditional cSLO designs employ separate optical paths for illumination and collected light [9], requiring separate confocal pinholes (or equivalently, fiber endfaces) in both the illumination and collection paths, each of which must be aligned, with five degrees of freedom, to be exactly conjugate to the other *and* the subject retina, all with micrometer-scale precision. Such precise alignment is achievable in a rigid tabletop setup but is difficult to maintain against the rigors of a portable, handheld form factor, which include mechanical shock and thermal cycling. We have previously attempted to construct a handheld cSLO probe using such a dual-path topology; despite initial success in alignment, after some use in handheld operation, collection efficiency degraded and it was necessary to frequently realign the collection fiber to maintain throughput.

In light of the above, in this work we choose to pivot from the traditional dual-path optical topology towards a less alignment-sensitive, single-path topology that leverages a double-clad fiber (DCF). A DCF is a type of specialty optical fiber that simultaneously guides light in both a singlemode core and a multimode inner cladding [10–12]. In our handheld HSS-SLO system, the core of the DCF is used to deliver illumination light to the patient interface, while the multimode inner cladding is simultaneously used to collect scattered light from the retina.

By using a DCF and a common optical path for illumination and collection in this manner, the single-path topology maintains good confocal alignment, even in the face of mechanical shock: it may be shown through an argument involving Helmholtz reciprocity, and an assumption of diffuse scattering at the retina, that such an arrangement is self-aligning in the lateral direction. Self-alignment in the axial direction is not similarly guaranteed, but due to the relatively low NA of the collection beam, there is inherently more tolerance for misalignment in this dimension.

However, the use of a DCF in a single-path topology tends to degrade signal-to-noise ratio (SNR) due to backreflections occurring at the glass-to-air interface at the DCF endface [13], which cause illumination light to back-couple into the inner cladding [14,15]. This backreflection causes leakage, or “crosstalk,” of illumination light from the source directly into the collected image signal, introducing both a constant background level and also photon shot noise. The impact of the constant background level can be mitigated electronically (e.g. by an analog summing amplifier prior to digitization), but the photon shot noise is stochastic and cannot be removed from the image signal. Therefore, reducing the DCF endface backreflection is crucial to achieving good SNR. Here we use the angled no-core fiber method presented by Malone et al. in [16] to reduce backreflections; in addition, we present a quantitative analysis of the degradation of optical SNR by added background level in order to guide future design efforts.

Along with maintaining good optical alignment, another critical aspect of cSLO design is the choice of a scan pattern for scanning the subject retina. Almost all existing point-scanning imaging systems, including cSLO and optical coherence tomography (OCT), employ a raster scan pattern, wherein many parallel scan lines of image data (i.e., reflectance measurements or A-scans) are acquired across the retina to digitally form an image. In addition to the fundamental, speed-limiting trade-off between slew rate and scanner turnaround present in any mechanical raster scanning system, raster scanning is also less than ideal for ophthalmic imaging. First, it is a poor fit to circular clear apertures—the rectangular outline of a raster scan either underfills or overfills the circular clear aperture of an imaging system, neither of which is desirable. Moreover, when a raster scan is performed with visible or pseudo-visible illumination (as is usually the case in SLO), subjects tend to perceive and track the moving “scan line” across their field of vision, thus introducing motion artifacts, such as described in [17].

In an effort to increase the frame rate of point-scanning imaging systems, previous work on non-raster scan patterns in OCT has explored Lissajous scanning [18,19] and constant angular velocity (CAV) spiral scanning [20]. However, both of these scan patterns suffer from a less than ideal sampling density distribution—a Lissajous pattern is denser at the periphery than the

center, and a CAV spiral grows increasingly sparse at larger radii, neither of which is desirable in retinal imaging, since clinically relevant information can be distributed widely across the retina. Recently, our group has introduced the use of constant linear velocity (CLV) spiral scanning to ophthalmic OCT [21], a technique which has precedent in atomic force microscopy (AFM) [22], another point-scanning imaging modality. In CLV spiral scanning, the angular speed of the spiral scan path is varied so as to maintain a theoretically constant linear velocity at all points throughout a scan. The CLV spiral method successfully addressed the sampling density falloff of the CAV spiral at large radii and improved performance over raster scanning [21]. However, a CLV spiral is still not completely optimal due to the singularity present at the center of the spiral pattern—a very high angular velocity (and thus scanner bandwidth) is required to maintain a constant linear velocity at small radii, and thus existing examples of CLV spiral scanning often suffer from distortions near the center of the image, where the scanners are unable to adhere to the commanded scan pattern [21,22].

In this paper, we present a hybrid spiral scanning SLO (HSS-SLO) system that introduces a “hybrid spiral” scan pattern to cSLO scanning. The hybrid spiral scan pattern is a hybridization of a CAV spiral with a CLV spiral, forming a scan pattern that combines the uniform sampling density of a CLV spiral with the well-behaved nature of a CAV spiral at small radii. The continuous, curvilinear nature of the spiral pattern overcomes the limitations of raster scanning by eliminating fast axis scanner turnaround, thus enabling image data collection with a nearly 100% duty cycle, all while reducing heat generation from mechanical scanners and more efficiently filling circular clear apertures. Additionally, the perceived bulls-eye shape of the scan pattern, when used under visible illumination, could potentially be leveraged as a fixation target for the subject. A similar approach of hybridizing CAV and CLV spiral scan patterns has been previously introduced in AFM [23], where the piezoelectric nanopositioners used for mechanical scanning are subject to similar constraints as the galvanometer scanners used in optical point-scanning.

Despite the advantages of a spiral scan pattern, the departure from traditional raster scanning complicates image reconstruction, since there is no longer a straightforward mapping from scan time to output pixel position. In the HSS-SLO system, we present a solution to this problem by recording the trajectory of the scanning mirrors during a scan, and then performing raster resampling by using an inverse-distance weight (IDW) interpolation algorithm [24]. For reconstructed images to be available for operator guidance during imaging, it was necessary for this resampling process to execute in faster than real time. In HSS-SLO, we performed significant optimization of the interpolation and resampling algorithms, including their implementation in CUDA C++ on an NVIDIA graphics processing unit (GPU), to sufficiently accelerate the image reconstruction process to meet this requirement.

## 2. Theory & methods

### 2.1. System design and form factor

The system diagram and optical layout of the complete HSS-SLO system with handheld probe are shown in Fig. 1 below. The system consists of a host PC running custom C++ software that interfaces with HSS-SLO optical engine, which contains the light source, tunable lens driver, beam scanning, and light detection subsystems. The HSS-SLO optical engine is coupled to the portable patient interface (probe) by a flexible tether carrying fiber optic and electrical cables.

For ease of use in the clinic, the entire HSS-SLO system was built into a mobile computer cart (Global Equipment Company Inc., Port Washington, NY) as shown in Fig. 2(a). To minimize its footprint, the HSS-SLO engine is integrated directly into an E-ATX computer chassis, alongside the computer components (Fig. 2(b)), and a custom-designed platform securely stores the portable probe when not in use.

Mechanical design of the handheld HSS-SLO probe (Fig. 2(c)) was performed in SolidWorks (Dassault Systèmes SolidWorks Corp, Concord, MA). Custom-designed mechanical components

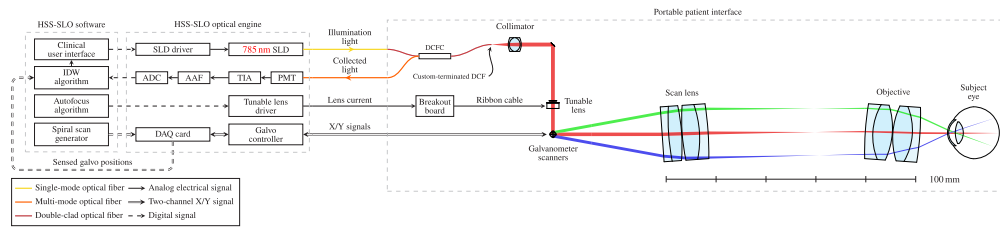


**Fig. 1.** HSS-SLO system diagram and optical layout. The green- and blue-shaded beams after the galvanometer scanners illustrate the paths taken by light when the galvanometer scanners are deflected  $\pm 10.3^\circ$  optical. This scan angle is angularly magnified  $2.4\times$  by a  $4f$  telescope to scan up to a  $50^\circ$  peak-to-peak visual angle (per the ISO 10940 definition) into the subject eye. Scattered light from the subject retina follows the same path as illumination light, in reverse, from the subject retina to the same specially terminated double-clad fiber from which the illumination light was launched. A double-clad fiber coupler extracts the collected light for detection and digitization. Images are acquired using a non-raster “hybrid spiral” scan pattern, which requires special image rasterization before display (see Section 2.3). AAF, anti-alias filter; ADC, analog-to-digital converter; DAQ, data acquisition; DCF, double-clad fiber; DCFC, double-clad fiber coupler; IDW, inverse distance-weighted interpolation algorithm; PMT, photomultiplier tube module; SLD, superluminescent diode; TIA, transimpedance amplifier.

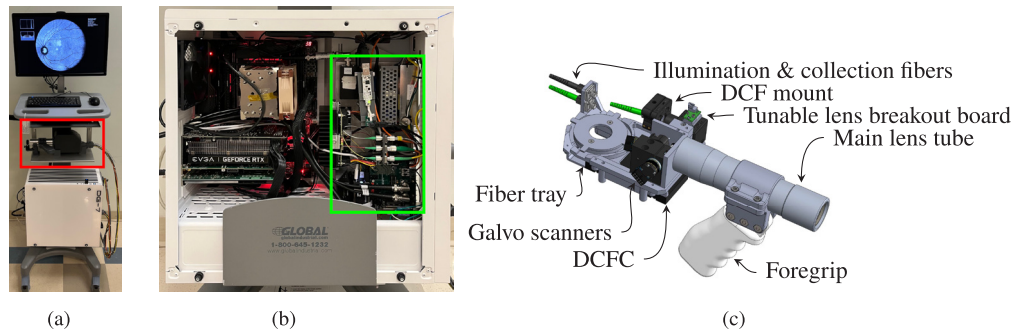


**Fig. 2.** (a) Photograph of the complete HSS-SLO system, mounted on a mobile computer workstation. Highlighted in red is the handheld probe on its storage platform. (b) Photograph showing the HSS-SLO optical engine (outlined in green) integrated inside the clinical computer chassis. (c) Rendering of the handheld HSS-SLO probe without its protective enclosure. DCF: double-clad fiber; DCFC: double-clad fiber coupler.

as well as lens and fiber mounts were fabricated on a commercial SLA 3-D printer (Form 3, Formlabs Inc., Somerville, MA) to allow the positioning of optical components at the required tilt angles, while larger optomechanical components were machined from aluminum alloy to maintain required dimensional tolerances and rigidity. In order to drive the probe's tunable lens, a custom  $13\text{ mm} \times 19\text{ mm}$  printed circuit board (see Fig. 2(c)) was designed to convert between the delicate flexible printed circuit (FPC) cable of the lens and a robust, overmolded cable assembly (Molex LLC, Lisle, IL). This cable carries the tunable lens drive current through the HSS-SLO probe's tether, which also contains cables carrying the X-Y galvanometer drive signals and fiber optic patch cords that convey illumination light from the engine and collected light from the probe (Fig. 1). Because of the limited length of its DCF output arm, the double-clad fiber coupler (DCFC) was located inside the HSS-SLO probe, where a custom 3-D printed fiber tray secures its fiber leads and also mounts two fiber mating sleeves for coupling light into and out of the

DCFC (Fig. 2(c)). In the current system, the large footprint of the DCFC's OEM packaging limited the degree of miniaturization that was achievable in the current iteration of the handheld HSS-SLO probe. In a future version, we hope that relocating the DCFC into the engine and optically coupling it to the probe through an extended length of DCF will significantly reduce the probe's footprint.

## 2.2. Optical design

The light source used in the HSS-SLO engine was a fiber-coupled superluminescent diode (SLD) operating at  $785.0 \pm 7.5$  nm (Superlum Diodes Ltd., Cork, Ireland). A double-clad fiber coupler (DC530SE, Castor Optics Inc., Saint-Laurent, Canada) couples illumination light into the singlemode core of a double-clad fiber (DCF), which then conveys the light to the probe through a flexible tether. At the distal end of the DCF, light launches into the relay optics through a custom high-angle termination designed to reduce backreflections, which is critical for SNR, as described in Section 2.2.1.

Design and optimization of the free-space relay optics was performed in OpticStudio (Zemax, Kirkland, WA). All optics used in the HSS-SLO probe are commercially available stock lenses. The input beam is first collimated by a Hastings triplet (TRH064-010-A, Thorlabs Inc., Newton, New Jersey), turned  $90^\circ$  by a fold mirror, and then refocused by an electrically tunable liquid lens (EL-3-10, Optotune AG, Dietikon, Switzerland) to compensate for subject refractive error before being scanned by a pair of X-Y galvanometer scanners (Saturn 1B, Pangolin Laser Systems Inc., Sanford, FL). The tunable lens was positioned as close as possible to the galvanometer mirrors to reduce beam clipping due to beam divergence. In HSS-SLO, the galvanometers execute a novel hybrid spiral scan pattern, as commanded by software running on the host PC (Section 2.3). After scanning, a  $4f$  telescope composed of two Plössl eyepieces, each of which consists of a pair of achromatic doublets (EFL = 60 mm and 25 mm for the scan lens and objective, respectively, giving  $60/25 = 2.4\times$  angular magnification), relays the illumination beam through the subject pupil at varying angles of incidence, from which it is brought to a focus at different spots on the retina, depending on the scan angle of the galvanometers. The two Plössl eyepieces of the telescope are tilted off-axis by  $4.0^\circ$  in opposite directions (Fig. 1) to reduce lens reflexes while preserving optical performance.

Performance of the relay optics is observed through simulated spot diagrams (Fig. 3), which indicate approximately  $30\ \mu\text{m}$  theoretical lateral resolution on the retina. Despite minor aberrations resulting from the tilted telescope lenses, which manifest as changing spot shapes across the horizontal axis of Fig. 3, the optical performance of the system remains diffraction-limited across the field of view. The illumination beam footprint at the pupil is approximately 0.65 mm in diameter on-axis, 1.0 mm across 70% of the scan angle, and 1.5 mm across the full  $50^\circ$  visual scan angle.

Light scattered from the retina propagates through the relay optics in reverse from the illuminated spot on the retina through the  $4f$  telescope, after which it is descanned by the galvanometers and is ultimately collected by coupling into the multimode inner cladding of the DCF. The focal length of the collimator (10 mm) and beam diameter (3.0 mm) combine to give an Airy disk diameter of  $6.4\ \mu\text{m}$  at the DCF endface. This Airy disk diameter is larger than the  $2.3\ \mu\text{m}$  core diameter of the DCF but smaller than the multimode inner cladding of the DCF, which has a  $15\ \mu\text{m}$  diameter, giving an effective pinhole size of 2.35 times the Airy disk diameter. The small diameter of the DCF inner cladding enables confocal rejection of out-of-focus light [9], thus reducing glare. The double-clad fiber coupler then extracts the collected light into a step-index multimode fiber (FG200LEA, Thorlabs, Newton, New Jersey), which guides it to a photomultiplier tube (PMT) for detection (H10721-20, Hamamatsu, Shizuoka-ken, Japan). After current-to-voltage conversion by a transimpedance amplifier (C9999-01, Hamamatsu, Shizuoka-ken, Japan), the image signal is then anti-alias filtered by a 2.5 MHz lowpass filter



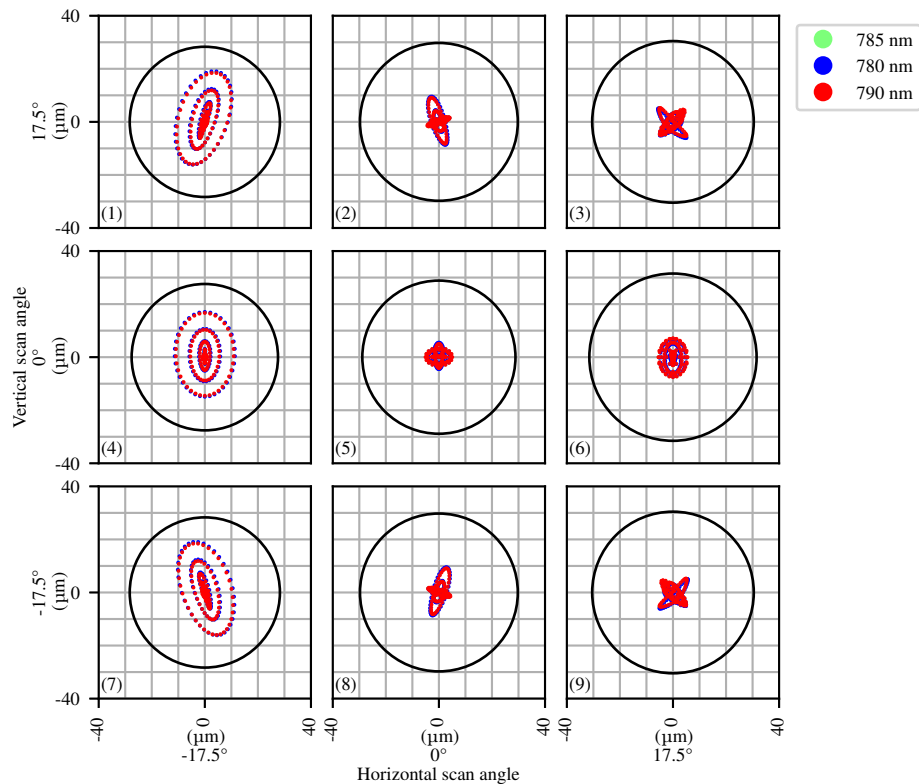


**Fig. 3.** Simulated spot diagrams produced by the handheld HSS-SLO system on the retina at regularly spaced points on a  $3 \times 3$  grid inscribed within the circular  $50^\circ$  visual angle field of view. Note that the four diagonal spots (1, 3, 7, and 9) are located  $\sqrt{2} \times 17.5^\circ \approx 24.75^\circ$  off-axis, near the edge of the field. The spots indicate diffraction-limited performance across the design field of view. The Airy radii (black circles) are approximately  $30 \mu\text{m}$ .

(BLP-2.5+, Mini-Circuits, Brooklyn, New York) before digitization at 10 MS/s with 12-bit resolution (ATS9130, Alazar Technologies Inc., Pointe-Claire, Canada). The values of the X-Y galvanometer position sensors throughout a frame are simultaneously digitized by a data acquisition card (PCIe-6363, National Instruments, Austin, TX) at 200 kS/s to aid in image reconstruction, as described in Section 2.3.2. Software running on the host PC then processes the incoming image and scanner response signals to produce images for real-time display. An intensity metric-based autofocus algorithm may be triggered by the operator via a foot pedal to automatically optimize image quality by sweeping the optical power of the tunable lens, as described in [25,26].

#### 2.2.1. Use of a double-clad fiber coupler in a single-path optical topology

The selection of a single-path optical topology leveraging a double-clad fiber for both illumination and light collection was driven by the need to ruggedize the system and minimize its sensitivity to mechanical shock. Past experience with handheld SLO designs has led us to the conclusion that a separate-aperture topology with separate illumination and collection light paths is challenging to use in a handheld probe, because even minor mechanical shock to the probe, or strain on the fibers leading to the probe can upset the delicate relative alignment required between the illumination and collection fibers. In this system, we opted instead to use a single DCF and a common optical path for both illumination and collection, as this arrangement guarantees that

the illuminated spot on the retina will always be imaged onto the collection aperture. In our architecture, the singlemode core of the DCF guides illumination light into the probe, and the outer multimode inner cladding conveys the signal light from the subject onto the detector.

In order to efficiently couple light into and out a DCF, we employ a double-clad fiber coupler (DCFC), which is a 3-port fiber optic network consisting of a DCF spliced to a step-index multimode fiber. (The unused end of the multimode fiber is terminated by the manufacturer with a high return-loss termination.) We will denote the DCF input port as 1, the DCF output port as 2, and the multimode collection port as 3, so that illumination light enters port 1 and is guided to port 2 via the DCF core, and collected light re-enters port 2 and is guided to port 3 via the multimode inner cladding.

In microwave circuit analysis, it is typical to use the *scattering matrix*, or *S*-matrix, to model multiport networks [27]. Similarly, we can model a DCFC as a polarization-insensitive, 3-port optical device with *S*-matrix:

$$S = \begin{bmatrix} S_{11} & S_{12} & S_{13} \\ S_{21} & S_{22} & S_{23} \\ S_{31} & S_{32} & S_{33} \end{bmatrix}$$

where each parameter  $S_{ij}$  is the electric field transmission coefficient from port  $j$  to port  $i$  [28], so the power transmittance ratio is then  $P_{i,\text{out}}/P_{j,\text{in}} = \|S_{ij}\|^2$ . Several of these *S*-parameters are critical to the function of the DCFC in an imaging application: an ideal DCFC would have  $S_{ij} = 0$  everywhere except for  $S_{21} = S_{32} = 1$ , thus enabling transmission from port 1 to port 2 and from port 2 to port 3 (Fig. 4). Real DCFCs exhibit non-ideal transmission loss, return loss, and crosstalk characteristics, some of which have significant impacts on system performance: non-infinite return loss at port 1 manifests as optical feedback ( $\|S_{11}\|^2 > 0$ ), which has the potential to destabilize sources. In practice, most sources are tolerant of some degree of feedback, so this is not a major concern. The multimode inner cladding transfer ratio is represented by  $\|S_{32}\|^2$ , which is always less than unity in a real device; the DCFC used in our system has a specified  $\|S_{32}\|^2 \geq 0.70$ . This nonideality results in collection losses and limits SNR, but its contribution is well understood.

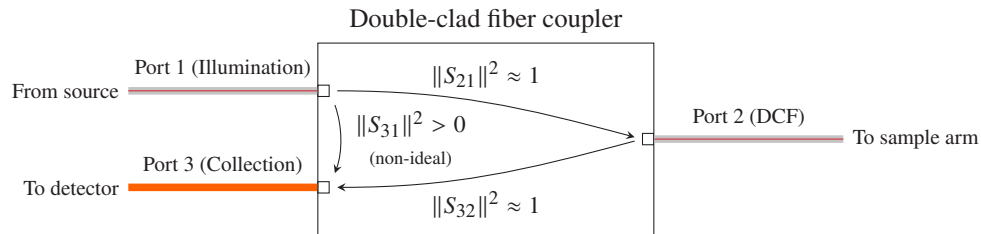


**Fig. 4.** A double-clad fiber coupler (DCFC), modeled at the network level as a 3-port device with power transmittance from port  $j$  to port  $i$  denoted as  $\|S_{ij}\|^2$ . In real DCFCs, due to backreflections occurring at the endface of port 2, there is unwanted light transmission (modeled by  $S_{31}$ ) from port 1 directly to port 3, negatively impacting sensitivity.

Far more problematic for an imaging application is the cross-transmittance, or “crosstalk,” from port 1 to port 3, denoted as

$$\|S_{31}\|^2 = \frac{P_{3,\text{out}}}{P_{1,\text{in}}}$$

where  $P_{3,\text{out}}$  is the optical power leaving port 3 resulting from power  $P_{1,\text{in}}$  incident upon port 1. For the remainder of this paper, we will make the simplifying assumption that  $\|S_{21}\|^2 = 1$  so that

$P_{1,\text{in}} = P_{2,\text{out}}$ , which allows us to define

$$\tau_{\text{dcfc}} \equiv \frac{P_{3,\text{out}}}{P_{2,\text{out}}} = \frac{P_{3,\text{out}}}{P_{1,\text{in}}}$$

as the crosstalk transmittance of the DCFC. The simplifying assumption above is motivated by a practical consideration: the assumption that  $\|S_{21}\|^2 = 1$  allows easy measurement of  $\tau_{\text{dcfc}}$  by measuring  $P_{2,\text{out}}$ , which can be measured in the free space after port 2, instead of  $P_{1,\text{in}}$ , which is measurable only by demating fibers. For a typical DCFC with a standard  $8^\circ$  FC/APC termination on port 2, we have measured  $\tau_{\text{dcfc}} = -39.0$  dB at  $\lambda = 785$  nm. However, because the optical power entering port 1 (from the source) is far greater than the collected power entering port 2, even small values of  $\tau_{\text{dcfc}}$  have a strong influence on the total power exiting port 3.

It is instructive to understand the underlying mechanism that produces DCFC crosstalk. According to Malone et al., crosstalk results from backreflections at the endface of the DCF sample port (port 2 in Fig. 4) [16]: light entering the DCFC at its input port is guided to the sample port, where a portion couples into free space as desired, but the remaining fraction is scattered at the air/glass interface present at the DCF endface. Some of this scattered light then couples into the multimode inner cladding of the DCF, where it is guided, along with collected retinal light, to exit the DCFC at port 3. Although this mechanism involves reflection at the endface of port 2, in the case of temporally incoherent illumination (e.g. the light produced by an SLD), it has the same effect at the network level as direct transmittance from port 1 to port 3.

This added background light from DCFC crosstalk is problematic in an imaging modality without coherence gating (such as SLO), since reduces the sensitivity of the system by contributing additive photon shot noise which competes with, and is indistinguishable from, the relatively weak retinal reflectance signal. A rigorous analysis of this impact on sensitivity and its dependence on the  $\tau_{\text{dcfc}}$  parameter is given below in Section 2.2.2.

In order to improve the sensitivity of our cSLO system, we experimented extensively with various methods of reducing DCF endface backreflections. The method giving the least backreflection, which was used in the HSS-SLO probe, was one developed by Malone et al.: a short length of no-core fiber (NCF) is fusion-spliced to the sample arm end of the DCF, and then the end of the NCF is epoxied in a ceramic ferrule and polished to a  $20^\circ$  angle [16]. The spatial offset and high angle of the NCF endface redirect the reflection of the cone of light launching from the singlemode core of the DCF away from the acceptance cone of the multimode inner cladding of the DCF. This termination method reduced the overall DCFC crosstalk level to  $\tau_{\text{dcfc}} = -48$  dB, a 9 dB improvement relative to a standard FC/APC termination. This reduction mitigated the impact of DCFC crosstalk on sensitivity, allowing us to leverage the mechanical robustness of a single-path DCFC topology while minimizing the impact on image SNR.

For further discussion of attempted and potential methods for reducing and managing DCFC crosstalk, see Section 4.1.

### 2.2.2. Impact of double-clad fiber coupler crosstalk on sensitivity

In order to analyze the impact of DCFC crosstalk on the sensitivity of the cSLO system, and hence the signal-to-noise ratio (SNR) of the images it produces, we model the imaging process, as shown in Fig. 5. The quantities which characterize system performance are as follows:  $\eta_{\text{fwd}}$ , the forward efficiency of the system is defined as  $\eta_{\text{fwd}} \equiv P_{\text{illum,obj}}/P_{\text{illum,fiber}}$ , where  $P_{\text{illum,obj}}$  is the illumination power leaving the objective, and  $P_{\text{illum,fiber}}$  is the illumination power entering the transfer optics. The reverse collection efficiency of the system is defined as  $\eta_{\text{rev}} \equiv P_{\text{sig,det}}/P_{\text{sig,obj}}$ , which is the proportion of light from the subject available at the objective which is ultimately incident upon the detector after passing through the transfer optics in reverse. The total crosstalk of the system is defined as  $\tau_{\text{cross}} \equiv \tau_{\text{dcfc}} + R_{\text{lenses}}$ , which accounts for both DCFC crosstalk and also internal Fresnel reflections from the lenses,  $R_{\text{lenses}}$ . The total power



incident upon the detector is defined as  $P_{\text{det}} \equiv P_{\text{sig,det}} + P_{\text{cross}}$ , where  $P_{\text{sig,det}}$  is as defined above, and  $P_{\text{cross}} = \tau_{\text{cross}} \cdot P_{\text{illum,fiber}} = \tau_{\text{cross}} \cdot P_{\text{illum,obj}}/\eta_{\text{fwd}}$  is the power incident upon the detector resulting from both DCFC crosstalk and lens reflections. For simplicity, we assume that each of these system quantities is invariant across scan angles and tunable lens powers.

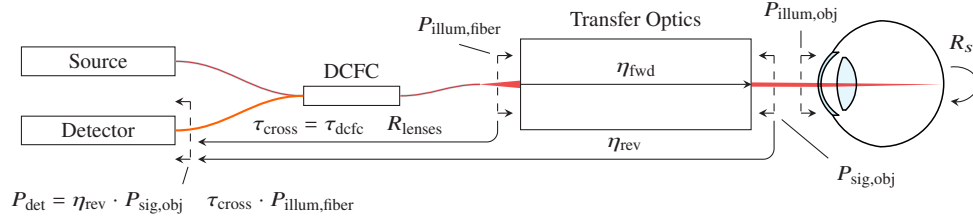


**Fig. 5.** Diagram showing the model used to analyze the sensitivity of our SLO system. Dashed lines indicate the power flow through the given surface in the direction of the arrowheads at the ends of the line. Solid arrows indicate the power transfer efficiency from the start to end point of the arrow, with the transmittance factor labeling the arrow. For example, the forward efficiency of the transfer optics is  $\eta_{\text{fwd}}$ , and so the optical power incident upon the subject eye is  $P_{\text{illum,obj}} = \eta_{\text{fwd}} \cdot P_{\text{illum,fiber}}$ .

In addition to the characteristics of the optical system itself, the imaging process also involves a finite pixel integration time  $\Delta t$ , which depends on both the scan pattern used and the resolution at which the image is ultimately rasterized (Section 2.3). Finally, the reflectance of the retina  $R_{\text{retina}}$ , and the reverse efficiency of the subject eye  $\eta_{\text{eye,rev}}$  combine to form the effective sample reflectance,  $R_s = R_{\text{retina}} \cdot \eta_{\text{eye,rev}}$ , thus determining the signal power leaving the subject eye as  $P_{\text{sig,obj}} = R_s \cdot P_{\text{illum,obj}} = (\eta_{\text{eye,rev}} \cdot R_{\text{retina}}) \cdot P_{\text{illum,obj}}$ .

Because the SLD source used in HSS-SLO has low temporal coherence, the photon flux incident on the photodetector can then be expressed as the direct sum of the signal and crosstalk flux:

$$\Phi_{\text{det}} = \frac{P_{\text{det}}}{h\nu} = \frac{P_{\text{illum,obj}} \cdot (R_s \cdot \eta_{\text{rev}})}{h\nu} + \frac{P_{\text{illum,obj}} \cdot \frac{\tau_{\text{cross}}}{\eta_{\text{fwd}}}}{h\nu} = \Phi_{\text{sig}} + \Phi_{\text{cross}}, \quad (1)$$

where  $\Phi_{\text{sig}}$  and  $\Phi_{\text{cross}}$  are the first and second terms of the middle expression, respectively, and  $h\nu = hc/\lambda$  is the photon energy at the operating wavelength.

The optical signal-to-noise ratio (SNR) of an optical signal is defined as the mean signal power to the noise standard deviation [29]. Because shot noise resulting from DCFC crosstalk (i.e. “crosstalk noise”) is the dominant noise source in the system in our operating regime, we will consider only the contribution of crosstalk noise and the shot noise of the image signal itself in this analysis. This analysis considers only optical SNR and neglects the contribution of detector noise, which is dependent on the specific detector used. Assuming that photon arrival times are uncorrelated, the shot noise of a signal with mean photon number  $N$  has a Poisson distribution with standard deviation  $\sqrt{N}$  [30]. The SNR of a single pixel with integration time  $\Delta t$  can then be written as:

$$\text{SNR} = \frac{\Delta t \cdot \Phi_{\text{sig}}}{\sqrt{\Delta t \cdot (\Phi_{\text{sig}} + \Phi_{\text{cross}})}} = \sqrt{\Delta t} \left( \frac{\Phi_{\text{sig}}}{\sqrt{\Phi_{\text{sig}} + \Phi_{\text{cross}}}} \right). \quad (2)$$

Each photon flux quantity in Eq. (2) can be more conveniently expressed in terms of the system parameters illustrated in Fig. 5. After simplification, this gives:

$$\text{SNR} = \sqrt{N} \cdot \frac{\eta_{\text{rev}} \cdot R_s}{\sqrt{\eta_{\text{rev}} \cdot R_s + \frac{\tau_{\text{cross}}}{\eta_{\text{fwd}}}}}, \quad (3)$$

where  $N = \Delta t \cdot P_{\text{illum,obj}}/h\nu$  is the photon number incident on the eye per output pixel.

SNR is a useful metric for quantifying the quality of images of a particular sample, but since it depends on the effective sample reflectance  $R_s$ , it does not measure intrinsic system performance. To remedy this, let us define the sensitivity of a system as the reciprocal reflectance of a sample that would give  $\text{SNR} = 1$  when imaged [31,32]. That is:

$$\Sigma \equiv \frac{1}{R_s} \Big|_{\text{SNR}=1}$$

For our system, we can calculate the sensitivity by solving Eq. (3) for  $R_s$  such that  $\text{SNR} = 1$  and taking the reciprocal, giving:

$$\Sigma = \frac{2N\eta_{\text{rev}}}{1 + \sqrt{1 + \frac{4N\tau_{\text{cross}}}{\eta_{\text{fwd}}}}} \quad (4)$$

Inspection shows that the functional form of this equation is intuitively correct; in the limit, sensitivity increases with both illumination photon count and reverse efficiency. A plot of the sensitivity over a wide range of illumination power is given in Fig. 6.

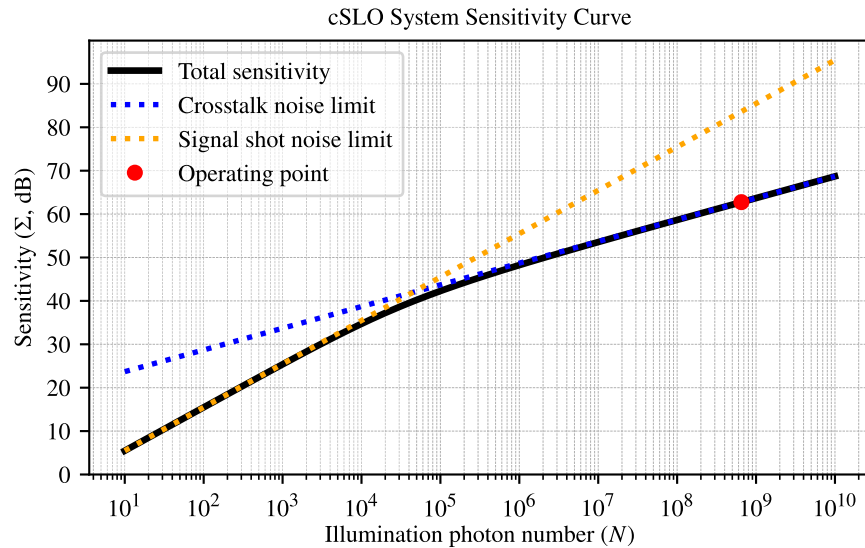


**Fig. 6.** Sensitivity of the cSLO system as a function of illumination photon number  $N = P_{\text{illum,obj}} \cdot \Delta t / h\nu$ , according to Eq. (4). The sensitivity limits imposed by signal shot noise and crosstalk noise are shown as dotted lines. In our operating regime, the overall sensitivity is primarily limited by shot noise arising from DCFC crosstalk.

In practice, each of the system parameters in Eqs. (2)–(4) straightforward to measure, except for  $\eta_{\text{rev}}$ . To measure  $\eta_{\text{rev}}$ , we placed a cat-eye retroreflector, consisting of a mirror placed in the focal plane of a lens, directly after the system objective. The retroreflector tilt and focal length were adjusted to optimize the incident power at the detector  $P_{\text{det}}$ , and then the approximation  $R_s \approx 1$  (assuming perfect retroreflectance) allowed the reverse efficiency to be calculated with the relation  $\eta_{\text{rev}} \approx P_{\text{det}} / P_{\text{illum,obj}}$ . The contribution of crosstalk was neglected for this calculation because it has negligible impact with a strongly reflecting sample.

Using this method, we measured the system parameters of the cSLO probe (with the custom high-angle DCF termination described in Section 2.2.1) to be:  $\eta_{\text{fwd}} = 0.697$ ;  $\eta_{\text{rev}} = 0.353$ ;  $R_{\text{lenses}} = -64.03$  dB;  $\tau_{\text{dcfc}} = -48.12$  dB;  $\tau_{\text{cross}} = -48.01$  dB. Our typical operating parameters

are  $P_{\text{illum,obj}} = 550 \mu\text{W}$  at  $\lambda = 785 \text{ nm}$  and  $\Delta t = 300 \text{ ns}$ , giving  $N \approx 6.5 \times 10^8$ , and a total sensitivity of  $\Sigma_{\text{dB}} = 62.75 \text{ dB}$  according to Eq. (4). (Both SNR and sensitivity are power ratios, so their decibel values are calculated as  $\text{SNR}_{\text{dB}} = 10 \cdot \log_{10} \text{SNR}$  and  $\Sigma_{\text{dB}} = 10 \cdot \log_{10} \Sigma$ , respectively.) This operating point is plotted in Fig. 6. In this operating regime, crosstalk-induced shot noise is the dominant noise source, as can be seen by the limiting lines in Fig. 6.

This sensitivity value is low compared to typical FD-OCT systems [31,32] because of the added shot noise contribution of DCFC crosstalk, but this is less impactful in confocal SLO, because it is a weakly axially-resolved modality that integrates sample reflectance across its depth of focus in the sample.

Additionally, with knowledge of  $\eta_{\text{rev}}$ , we are able to estimate the average of  $R_s$  across a subject retina as  $\overline{R_s} = \overline{P_{\text{sig,det}}} / (\eta_{\text{rev}} \cdot P_{\text{illum,obj}})$ , where  $\overline{P_{\text{sig,det}}}$  is measured with a low bandwidth limit in order to estimate the average sample reflectance. With the system scanning a  $50^\circ$  field of view, we estimated a typical value  $\overline{R_s} \approx -48.5 \text{ dB}$  for a healthy, non-mydratic human eye in dark conditions. This value in Eq. (2) gives  $\text{SNR} = 13.8 \text{ dB}$ .

The loss in optical SNR due to DCFC crosstalk may be quantified as  $L = \text{SNR}_{\text{dcfc}} / \text{SNR}_{\text{ideal}}$ , where  $\text{SNR}_{\text{dcfc}}$  is the optical SNR of our current system, and  $\text{SNR}_{\text{ideal}}$  is the optical SNR of a system with zero DCFC crosstalk (so that  $\tau_{\text{cross}} = R_{\text{lenses}}$  alone). For our system,  $\text{SNR}_{\text{dcfc}} = 13.8 \text{ dB}$  for a typical retina with  $\overline{R_s}$  as described above, and  $\text{SNR}_{\text{ideal}} = 17.3 \text{ dB}$ , so our loss factor is  $L = -3.5 \text{ dB}$ . In order for our system to achieve the same optical SNR as an ideal system with zero DCFC crosstalk, the quantity  $N = \Delta TP_{\text{illum,obj}} / h\nu$  must be increased by a factor of  $(1/L)^2 = 7 \text{ dB} = 5.0\times$  (the square compensates for the square root in Eq. (3)), either by increasing integration time, illumination power, or both.

Although this analysis has shown that the use of a DCFC is detrimental to image SNR and system sensitivity due to the presence of crosstalk-induced shot noise, we still believe that the use of a DCFC is warranted in this system, as the advantages it confers in mechanical robustness (in a handheld device) outweigh the reduction in SNR, which can be compensated for through multi-frame registration and averaging.

### 2.3. Hybrid spiral scanning

#### 2.3.1. Hybrid spiral scan pattern

At the core of the HSS-SLO system is the hybrid spiral scan pattern, which is executed by a X-Y galvanometer scanner pair that is capable of executing arbitrary scan waveforms within its bandwidth and slew rate limitations. The hybrid spiral is an Archimedean spiral parameterized in time in a piecewise fashion, so that the inner portion maintains constant angular velocity (CAV), while the outer maintains constant linear velocity (CLV). This hybridization depending on scan region ensures that the bandwidth limit of the galvanometer scanners is respected in the inner CAV region, and that uniform sampling density is maintained in the outer CLV region. The locations of the CAV and CLV regions can be seen in the color-coded plot of a hybrid spiral scan pattern in Fig. 7.

The equations describing a hybrid spiral scan pattern were derived by starting with the equations for CLV spiral scanning [21,22]. The theoretical scanner bandwidth required to execute a CLV spiral approaches infinity at the center of the pattern, which can induce unwanted scanner transients and introduce warping artifacts in the resulting images. While [22] describes a transfer function-inversion technique for shaping the CLV waveform to result in a higher-fidelity execution of the CLV spiral scan, we take a simpler, direct approach wherein the CLV spiral scan pattern is modified to insert a CAV segment at the center of the scan, thus sidestepping the CLV singularity altogether. The result is the hybrid spiral scan, which hybridizes a CAV spiral with a CLV spiral. Its parameterization is presented here in terms of volts in order to facilitate waveform generation, but the result is unit-agnostic.

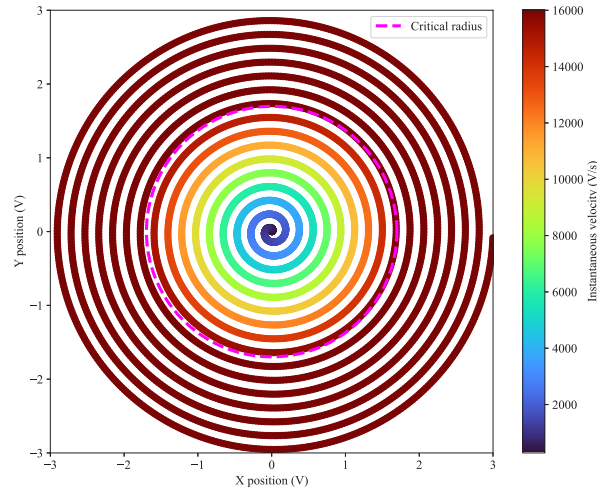


**Fig. 7.** Plot of an example hybrid spiral scan pattern with a 32-line cross-section (or 16 full loops). The color of each point indicates the instantaneous linear velocity (or equivalently, voltage slew rate) of the scan beam at that point. The scan pattern maintains constant angular velocity (CAV) near the center until it reaches the critical radius (dashed circle), where it transitions to constant linear velocity (CLV) for the remainder of the scan. A CAV spiral is bandlimited in the center, while a CLV spiral provides uniform sampling density in the outer annulus. The bulls-eye shape also acts as a natural fixation target when used under visible illumination, thus reducing motion artifacts. In practice, the actual HSS-SLO implementation uses far denser scan patterns, with a 534-line cross-section (267 full loops) being typical.

The hybrid spiral scan pattern is parameterized by several quantities. First, the intrinsic properties of the galvanometer scanners are captured as the bandwidth limit (in rad/s, denoted as  $\omega_{\max}$ ), and the slew rate limit (in V/s, denoted as  $v_{\max}$ ). Next, the radial extent and density of the desired scan pattern are described by the outside radius  $R_{\max}$  and the radial pitch  $\Delta R$  (both in V). The maximum radial extent  $R_{\max}$  is limited by the field of view of the optical system. For a critically sampled image, the radial pitch  $\Delta R$  was chosen to produce a lateral deflection at the retina approximately equal to the 30  $\mu\text{m}$  lateral resolution of our illumination optics.

From these four initial parameters, the following derived values are computed:

$$T_c = \frac{2\pi v_{\max}}{\omega_{\max}^2 \Delta R} \quad (5)$$

$$R_c = \frac{v_{\max}}{\omega_{\max}} \quad (6)$$

$$\Delta T = T_c - \frac{\pi R_c^2}{v_{\max} \Delta R} \quad (7)$$

$$T_{\text{end}} = \frac{\pi R_{\max}^2}{v_{\max} \Delta R} + \Delta T \quad (8)$$

$$N_{\text{loops}} = R_{\max} / \Delta R \quad (9)$$

These are the critical time  $T_c$  and critical radius  $R_c$  at which the CAV/CLV transition occurs; the CLV delay time  $\Delta T$ , which is the time shift required to align the CAV and CLV segments; the

total duration of the scan  $T_{\text{end}}$ ; and the number of loops  $N_{\text{loops}}$ . With these values, hybrid spiral scan pattern may be described in polar form:

$$R(t) = \begin{cases} t \cdot \frac{\Delta R \omega_{\text{max}}}{2\pi} & \text{if } t < T_c \\ \sqrt{\frac{v_{\text{max}} \Delta R (t - \Delta T)}{\pi}} & \text{if } T_c \leq t \leq T_{\text{end}} \end{cases} \quad (10)$$

$$\theta(t) = \begin{cases} t \cdot \omega_{\text{max}} & \text{if } t < T_c \\ \sqrt{\frac{4\pi v_{\text{max}} (t - \Delta T)}{\Delta R}} & \text{if } T_c \leq t \leq T_{\text{end}} \end{cases} \quad (11)$$

For an outward-spiraling scan, the exact X- and Y-axis galvanometer drive waveforms are then:

$$X(t) = R(t) \cos \theta(t). \quad (12)$$

$$Y(t) = R(t) \sin \theta(t). \quad (13)$$

The time parameter  $t$  ranges as  $0 \leq t \leq T_{\text{end}}$ . For an inward spiral, the waveforms may be time-reversed as  $X'(t) = X(T_{\text{end}} - t)$  and  $Y'(t) = Y(T_{\text{end}} - t)$ .

Repeated spiral scanning requires a closed scan trajectory. The simplest option, which is taken in our implementation, is to insert a brief linear flyback segment to recenter the scanners after each frame. Alternating inward and outward spirals are also possible, but we chose not to pursue this route due to the marginal benefit it would yield: for a typical outwards-only scan, the spiral flyback and A/D rearm time consumes only 339  $\mu\text{s}$ , giving an acquisition duty cycle of 99.89%.

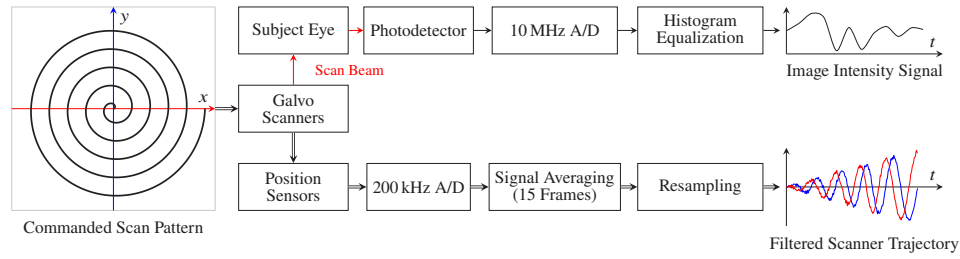
### 2.3.2. Real-time raster image reconstruction

In the HSS-SLO system, image reconstruction is necessary to convert 1-D intensity profiles acquired over the subject retina in the hybrid spiral scan pattern into 2-D raster images suitable for image processing and display. Moreover, this reconstruction should execute in real time to enable live image display for operator guidance during handheld imaging.

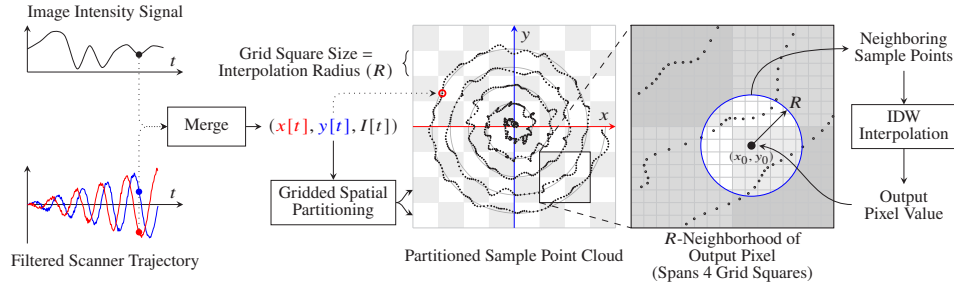
The complete HSS-SLO image acquisition and raster image reconstruction pipeline is illustrated in Fig. 8. During implementation of the HSS-SLO system, we found that it was not sufficient to assume that the galvanometer scanners execute the commanded scan pattern with absolute fidelity, so in the acquisition stage, both the image intensity signal and galvanometer position sensor values are simultaneously digitized (Fig. 8(a)). Separate analog/digital (A/D) converters were used for the image signal and scanner trajectory: the image signal was digitized by a 10 MHz ATS9130 PCIe A/D card (Alazar Technologies Inc, Pointe-Claire, Canada), while the dual-axis galvanometer position sensor signals were digitized at 200 kHz by a PCIe-6363 data acquisition card (National Instruments, Austin, TX). The use of separate digitizers at different sampling rates made it necessary to linearly interpolate and upsample the position sensor signals to match the image signal sampling rate. After upsampling, clock skew between the two digitizers was observed, so phase locking the two digitizer clocks was attempted but proved complicated in practice. Instead, we chose to perform a one-time calibration by measuring the relative frequency error between the two oscillators to be 12 ppm (which is within the manufacturing tolerance of typical commercial quartz crystal oscillators). This value was then used to perform software resampling to compensate for the observed clock skew, under the assumption that the relative frequency error would remain constant over time.

Power-law weighted histogram equalization is performed on the image signal at acquisition time (Fig. 8(a)) to enhance contrast by using an algorithm derived from ImageJ [34]. Noise in the position sensor trajectories was reduced by signal averaging [35] across the 15 most recent frames, under the assumption that the repeated executions of the same commanded waveform should result in similar measured trajectories. The origin of this noise was uncertain: it was unclear whether it was real or an artifact of the sensing and digitization process. (In a future





(a) Signal paths during HSS-SLO image acquisition.



(b) Flow diagram of GPU-accelerated HSS-SLO rasterization process.

**Fig. 8.** HSS-SLO image acquisition and real-time rasterization process. (a) First, during the acquisition stage, the two-dimensional trajectory taken by the galvanometer scanners (bottom row) is digitized alongside the image signal (top row). Double lines indicate a two-channel electronic signal. Red lines indicate an optical signal. (b) Next, the scanner trajectory is merged with the image signal to form a two-dimensional sample point cloud, wherein each sample point is paired with a corresponding image signal intensity. As an optimization for nearest-neighbor lookup, the sample points in this cloud are then spatially binned according to a regular grid [33]. Finally, gray levels for every pixel in the output are computed by inverse-distance weighted (IDW) interpolation across nearby sample points. The data shown are fully synthetic, and position noise has been exaggerated for illustration purposes.

system, we believe that directly interfacing via a digital protocol with the galvanometer servo driver could perhaps alleviate this noise.) The result of the image acquisition stage is an image intensity signal  $I[t]$ , along with filtered and resampled scanner trajectories  $x[t]$  and  $y[t]$ .

The measured image intensity signal and scanner trajectories are used as inputs to the image reconstruction pipeline, which begins execution immediately after each frame has been digitized and preprocessed by the acquisition phase. First, the acquired intensity signal and scanner trajectory are merged to form a 2-D “sample point” cloud (Fig. 8(b)). The points in this cloud are then partitioned according to their position into regular square bins which tile the image plane. This partitioning strategy, which is known as “spatial hashing” in computer graphics, accelerates nearest-neighbor queries for arbitrary coordinates within the image [33]. Then, to compute the gray level of a pixel in the output image, its nearest-neighbor sample points are queried and filtered so that only those within a radius  $R$  remain. (The partitioning grid square side length is constrained to be  $2R$ , so that the  $R$ -neighbors of any point fall within at most 4 grid bins.) These are then used as inputs to an inverse-distance weighted (IDW) interpolation function, which computes a weighted average of the intensities associated with these sample points, where the weights are computed to be inversely proportional to a constant power  $p$  of the distance between the output pixel and sample point. Specifically, let  $I_i$  be the intensity at a particular neighboring sample point  $i$ , and let  $d_i < R$  be the Cartesian distance between that sample point and the center

of the output pixel at  $(x_0, y_0)$ . Then, the gray level of the output pixel is given by [24]:

$$\text{Output Pixel Level} = \text{IDW}(x_0, y_0) = \frac{\sum_{d_i < R} d_i^{-p} I_i}{\sum_{d_i < R} d_i^{-p}} \quad (14)$$

This equation essentially computes a weighted average of the neighboring sample point intensities  $I_i$ , with weights inversely proportional to a power  $p$  of the distances to the points  $d_i$ . The power parameter  $p > 0$  controls the smoothing applied by the interpolation; a typical value is  $p = 3$  was empirically chosen for HSS-SLO, favoring sharpness over smoothness. If  $p = 0$ , the formula degenerates to an arithmetic mean. For output pixels where  $d_i = 0$  for some  $i$ , the output value is set to  $I_i$  to prevent division by zero. The above interpolation is performed for every pixel coordinate on a regular grid, thus forming the output raster image.

Our choice of IDW interpolation over a more straightforward nearest-neighbor approach was informed by the decoupling between the regular output pixel grid and the non-gridded, largely irregular distribution of sample points. There may be zero, one, or many more sample points lying within the boundaries of an output pixel; our approach makes no assumptions about the distribution of sample points among output pixels. (There is an exception to this with regard to algorithmic performance—in the case of a pathological scan pattern having an extremely non-uniform distribution of sample points, our spatial partitioning optimization would degenerate to a linear search, with a corresponding decrease in performance.) When nearest-neighbor interpolation was attempted on our image data, it was found that sample points with outlying intensity values near the centers of output pixels would dominate the output value of those pixels, thus introducing salt-and-pepper noise across the resulting image. The smoothing effect of IDW interpolation was found to largely mitigate this noise.

Despite the rasterization process being agnostic to output resolution, it is still necessary to make a selection of an appropriate output resolution that is informed by the underlying scan pattern. In HSS-SLO, a typical hybrid spiral scan pattern was operated with a 534-line cross-section (or 267 full loops of the spiral scan), a value selected to give a radial pitch on the retina commensurate with the optical resolution of our system (Sec. 2.3.1). Our final rasterization resolution was set to be  $1200 \times 1200$  px, approximately double the radial resolution in each dimension. This doubling was, in turn, motivated by knowledge of the anisotropy of our sample point cloud—due to the high digitization rate of our image signal (10 MHz, see Fig. 8(a)) and the relatively slower slew rate of our galvanometer scanners, our sample point cloud is oversampled along the direction of the spiral scan (i.e. azimuthally), and thus undersampled in the radial direction. Our choice of resolution at  $1200 \times 1200$  px thus allowed a compromise between the relatively low radial resolution and high azimuthal resolution of our sample point cloud.

In our HSS-SLO implementation, the signal preprocessing steps shown in Fig. 8(a) and the spatial partitioning step shown in Fig. 8(b) are performed by custom C++ software executing on an 10-core, 3.70 GHz Intel Core i9-10900K CPU. To improve performance, the IDW interpolation step is implemented in CUDA C++ on an NVIDIA RTX 3060 GPU (NVIDIA Corporation, Santa Clara, CA). Both steps take place live during the imaging process, and both execute faster than real time: for a typical scan with  $3 \times 10^6$  sample points, the time taken for preprocessing was measured to be 29 ms, and the rasterization step took 64 ms, for a total of 93 ms, whereas the scan itself takes 296 ms.

### 2.3.3. Registration & post-processing

After acquisition, SLO images are rasterized, and the best frames in the capture are selected for non-rigid registration by the MATLAB “imregdemos” algorithm [36,37]. Frame selection is currently performed manually but may be automated in future work, perhaps with the aid of a machine learning model. Saturated regions in each frame (e.g., those resulting from reflex

artifacts) are automatically located by thresholding and masked; after registration, the stack is then flattened with an outlier-discarding mean; and finally, the resulting image is homogenized to reduce vignetting. Motion in the underlying capture allows saturated regions to be partially or fully filled in by the registration process.

### 3. Results

#### 3.1. Human imaging

Feasibility of the use of the handheld HSS-SLO system in screening applications was demonstrated by imaging the retinas of eight adult volunteers with diabetes mellitus (irrespective of any history of diabetic retinopathy) during routine eye exams. The study was conducted under a protocol approved by the Duke University Health System Institutional Review Board and in accordance with the tenets of the Declaration of Helsinki. Optical power of the SLO beam was set to be  $400\ \mu\text{W}$  and verified on a calibrated power meter prior to each imaging session. This power level is well within the Group 1 limits of ANSI Z80.36-2021 for the 785 nm operating wavelength.

Informed consent was obtained from each subject. To faithfully gauge non-mydratiac performance, imaging was performed prior to the administration of any dilating drops that may have been associated with routine care. During each imaging session, the subject remained seated in a chair in a moderately darkened room. The operator stood in front of the subject and aligned

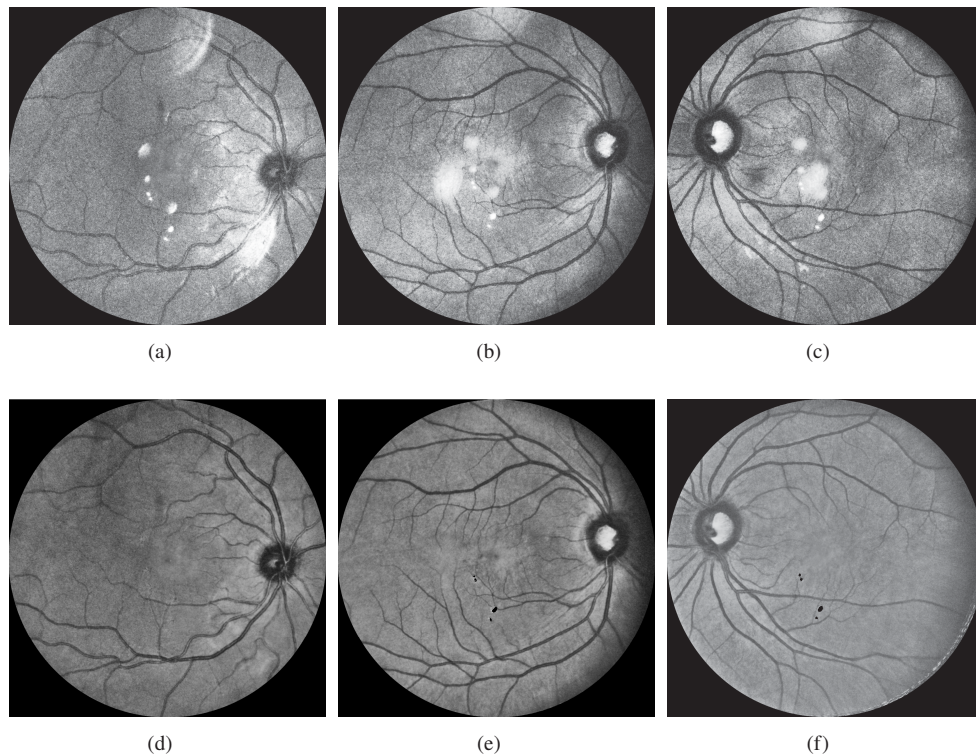


**Fig. 9.** Exemplary retinal images from two adult volunteers. Field of view is  $50^\circ$  (visual angle). (a)-(c) Single frames selected from HSS-SLO video, each acquired in 296 ms. (b) and (c) are of the two retinas of the same subject. (d)-(f) Nine-frame averages of frames from the subjects shown in (a)-(c), after non-rigid registration, background subtraction, and image homogenization. Note the reduction in noise from the upper row to the lower row, due to signal averaging.

the probe to one of the subject's eyes, using feedback from a live SLO video feed displayed on a monitor behind the subject. The subject was instructed to fixate on the center of the spiral scan pattern (which was dimly visible due to the near-infrared operating wavelength), and image data was saved once good alignment was achieved. The process was then repeated with the contralateral eye. Alignment was straightforward due to the small beam footprint at the pupil.

Images were acquired using a hybrid spiral scan pattern spanning a  $50^\circ$  field of view (visual angle) with a 534-line cross-section (267 full loops). Each raw frame was composed of approximately 3 million data points and acquired in 296 ms. Once acquired, images were registered and post-processed according to the process described in Sec. 2.3.3.

Exemplary images, both raw and post-processed, are shown in Fig. 9. Raw images shown in Figs. 9(a)–9(c) are single frames, and processed images shown in Figs. 9(d)–9(f) are nine-frame averages. The bright point artifacts visible in the single frames, resulting from internal lens reflections, are background-subtracted and almost entirely filled by the multi-frame registration process (Sec. 2.3.3). However, due to the fixation effect of the spiral scan (explored thoroughly in [38]), there was often insufficient motion between frames to completely fill in the saturated areas, resulting in the small black artifacts visible in Fig. 9(e)–9(f). These artifacts can be mitigated in future work through polarization gating, the use of custom optics optimized to minimize backreflections, or by dithering the center of the spiral scan slightly between scans.

## 4. Discussion

We have demonstrated several techniques useful for implementing confocal SLO in a handheld form factor. We have presented a thorough analysis of the effects of DCF backreflections on SLO image SNR, as well as a method for reducing its impact. Additionally, we have introduced the hybrid spiral scan pattern to confocal SLO as a novel technique for increasing acquisition efficiency over traditional raster scanning. The hybrid CAV/CLV time parameterization introduced by the hybrid spiral pattern eliminates the singularity at the center of the CLV spiral, thus combining the uniform sampling density of a CLV spiral with the distortion-free CAV spiral at small radii. The use of spiral scanning in SLO under visible illumination may also present advantages in terms of subject fixation, a phenomenon which we have initially explored in [38]. In a forthcoming paper, we intend to further investigate this observed fixation advantage of spiral scanning in ophthalmic imaging.

As discussed in Sec. 2.3.2, the rasterization process presented there is agnostic to the underlying scan pattern density. Moreover, it is also agnostic to the *scan pattern itself*! Although Fig. 8 illustrates the use of a spiral scan, at no point in the image reconstruction process is any assumption made about the shape of the underlying scan pattern—it could be a spiral, a raster, a Lissajous figure, or any other shape. Approaches similar to ours could thus enable the use of nearly arbitrary scan patterns in future point-scanning imaging systems, including SLO and also other modalities, such as OCT. In fact, we have already applied the HSS-SLO image reconstruction algorithm to the unwarping and dezippering of bidirectional resonant raster-scanned SLO images in the work described in [38].

### 4.1. Potential methods to further manage double-clad fiber backreflections

The high-angle, no-core fiber termination scheme used at our DCF endface yielded a 9 dB reduction in backreflection as measured relative to an  $8^\circ$  FC/APC termination directly on the DCF. This was less of an improvement than measured by Malone et al. in [16]. We speculate that this was perhaps the result of excess light being launched into the multimode inner cladding of the DCF at port 1 (see Fig. 4), since we employed a mechanical fiber mating sleeve to couple light from the SM fiber-pigtailed source into the DCFC. Core misalignment and mode field diameter (MFD) mismatch at the SMF-DCF joint could have contributed to this miscoupling.



We also observed that this SMF-DCF joint was especially sensitive to misalignment—the degree of backreflection could vary significantly depending on the state of the joint. We attempted to mitigate this by fusion splicing a length of SMF to the DCF input port, instead of using a mechanical mating sleeve. However, we did not observe a significant improvement, perhaps due to the same core misalignment and/or MFD mismatch issues that arose with the fiber mating sleeve. Finally, since the DCFC was located in the handheld portion of the system, this fiber joint was necessarily located there as well (transition between “Illumination light” and DCFC in Fig. 1, and Fig. 2(c)), where it was more susceptible to mechanical strain from the tether, which could also upset the alignment of the joint, reducing throughput and increasing crosstalk by altering the launch conditions into the DCFC. In effect, the requirement for precise alignment was shifted from the free-space optics of the handheld probe to this SMF-DCF joint. In future work, this issue of SMF-DCF alignment sensitivity could perhaps be mitigated by more successful fusion splicing. Moreover, this issue could potentially be eliminated altogether by relocating the DCFC into the system’s optical engine, where it would be protected from mechanical strain. This latter option has the added benefit of also miniaturizing the probe footprint, as described in Sec. 2.1.

In addition to the high-angle, no-core fiber approach described in Sec. 2.2.1, some other methods of mitigating the effect of DCF backreflections on SNR were either attempted or explored. Antireflection coating of the DCF endface was attempted through a commercial vendor but proved unsuccessful, perhaps due to the large NA of (and the resulting high incidence angles of light propagating through) the multimode inner cladding of the double-clad fiber. Despite our lack of success in further reducing the degree of DCFC crosstalk, current development in both academia and industry promises to improve the situation in the future, at which point the sensitivity drawbacks of the single-path optical topology presented here may perhaps be ameliorated.

Finally, a method to temporally gate the DCF endface backreflection was explored but not attempted. In this proposed technique, the SLD light source would be replaced by a fast pulsed laser, and the detector bandwidth would be increased to the GHz regime. Then, the free space after the DCF launch into air would be leveraged to introduce a delay between the arrivals at the detector of the backreflected pulse and the pulse scattered from the subject retina. Synchronizing the detector with the laser pulse repetition rate could then enable digital processing to separate the backreflected pulses from the signal pulses. Non-uniform pulse energy could be compensated for by measuring the energy of each pulse and normalizing the signal intensity values. Alternatively, a very fast multimode optical switch could be synchronized to the pulse train and clocked to allow only the signal light to pass. This would shift the requirement for high bandwidth from the detector to the switch. However, to the best of our knowledge, such fast multimode optical switches are not readily available. The length of the free space and modal dispersion in the DCF would drive the required pulse width and detector bandwidth. The requirement for high bandwidth could be reduced by lengthening the free space path after the DCF launch; however, this is at odds with the requirements of a handheld form factor. Tabletop systems which already incorporate long free-space sample arms, such as adaptive optics SLO, may be more suitable candidates for this approach. This approach was not attempted at this time due to its high cost, but future advances in fast multimode switches and detectors may make its implementation feasible.

## 5. Conclusion

We have introduced the theory and methods for implementing a double-clad fiber-based hybrid spiral scanning SLO (HSS-SLO) system in a handheld form factor. *In vivo* retinal imaging was performed with the handheld HSS-SLO system to demonstrate its feasibility.

**Funding.** National Institutes of Health (R01-EY030490, R01-EY031769, R01-EY033969, R21-EY030270, R21-EY033515).



**Acknowledgments.** The authors are deeply indebted to Richard Nappi and Bernie Jelinek for advice on mechanical fabrication, and to Michael Giacomelli, Pablo Ortiz, and Robert Trout for fruitful discussions. Mark Draelos co-developed the program that generated the optical diagrams in Figs. 1 and 3 from a Zemax file. This tool will soon be made freely available as open-source software.

Portions of this work were presented at the ARVO Annual Meeting in 2021, and the SPIE Ophthalmic Technologies XXXII & XXXIII Conferences in 2022 and 2023.

**Disclosures.** FW: Duke University (P), CV: Duke University (P), YKT: Vanderbilt University (P), ANK: Duke University (P), JAI: Duke University (P), AHD: Duke University (P).

**Data availability.** Data underlying the results presented in this paper are not publicly available at this time but may be obtained from the authors upon reasonable request.

## References

1. R. H. Webb and G. W. Hughes, "Scanning laser ophthalmoscopy," *IEEE Transactions on Biomedical Engineering* (1981), pp. 488–492.
2. R. H. Webb, G. W. Hughes, and F. C. Delori, "Confocal scanning laser ophthalmoscopy," *Appl. Opt.* **26**(8), 1492–1499 (1987).
3. D. S. Fong, L. Aiello, T. W. Gardner, G. L. King, G. Blankenship, J. D. Cavallerano, I. Ferris, L. Fredrick, and R. Klein, and for the American Diabetes Association, "Retinopathy in Diabetes," *Diabetes Care* **27**(suppl\_1), s84–s87 (2004).
4. J. M. Saari, P. Summanen, T. Kivelä, and K. M. Saari, "Sensitivity and specificity of digital retinal images in grading diabetic retinopathy," *Acta Ophthalmol. Scand.* **82**(2), 126–130 (2004).
5. K. Yogesan, I. J. Constable, C. J. Barry, R. H. Eikelboom, I. L. McAllister, and M.-L. Tay-Kearney, "Telemedicine screening of diabetic retinopathy using a hand-held fundus camera," *Telemedicine J.* **6**(2), 219–223 (2000).
6. A. Matimba, R. Woodward, E. Tambo, M. Ramsay, L. Gwanzura, and S. Guramatunhu, "Tele-ophthalmology: Opportunities for improving diabetes eye care in resource- and specialist-limited sub-saharan african countries," *J. Telemed. Telecare* **22**(5), 311–316 (2016). PMID: 26407990.
7. W. Zhang, P. Nicholas, S. G. Schuman, M. J. Allingham, A. Faridi, T. Suthar, S. W. Cousins, and S. G. Prakashaporn, "Screening for diabetic retinopathy using a portable, noncontact, nonmydriatic handheld retinal camera," *J. Diabetes Sci. Technol.* **11**(1), 128–134 (2017).
8. B. Cochener, "Suitability of a low-cost, handheld, non-mydratic retinograph for diabetic retinopathy diagnosis," *Investigative Ophthalmology & Visual Science* **57**(12), 6319 (2016).
9. F. LaRocca, A.-H. Dhalla, M. P. Kelly, S. Farsiu, and J. A. Izatt, "Optimization of confocal scanning laser ophthalmoscope design," *J. Biomed. Opt.* **18**(7), 076015 (2013).
10. C. Boudoux, L. Majeau, K. Beaudette, and N. Godbout, "Multimode and double-clad fiber couplers for biomedical optics," in *Applied Industrial Optics 2019*, (Optica Publishing Group, 2019), p. W2A.3.
11. K. Beaudette, N. Godbout, and C. Boudoux, "Advances in multimodal imaging using double-clad fiber couplers," *J. Lightwave Technol.* **37**(22), 5674–5685 (2019).
12. C. Boudoux, N. Godbout, and S. Lemire-Renaud, "Double clad fiber coupler and device," (2014). US Patent 8,792,757.
13. P. M. Lane, "Terminal reflections in fiber-optic image guides," *Appl. Opt.* **48**(30), 5802–5810 (2009).
14. J. D. Malone, M. T. El-Haddad, I. Bozic, L. A. Tye, L. Majeau, N. Godbout, A. M. Rollins, C. Boudoux, K. M. Joos, S. N. Patel, and Y. K. Tao, "Simultaneous multimodal ophthalmic imaging using swept-source spectrally encoded scanning laser ophthalmoscopy and optical coherence tomography," *Biomed. Opt. Express* **8**(1), 193–206 (2017).
15. M. T. El-Haddad, I. Bozic, and Y. K. Tao, "Spectrally encoded coherence tomography and reflectometry: Simultaneous en face and cross-sectional imaging at 2 gigapixels per second," *J. Biophotonics* **11**(4), e201700268 (2018).
16. J. D. Malone, M. T. El-Haddad, S. S. Yerramreddy, I. Oguz, and Y. K. K. Tao, "Handheld spectrally encoded coherence tomography and reflectometry for motion-corrected ophthalmic optical coherence tomography and optical coherence tomography angiography," *Neurophotonics* **6**(04), 1–11 (2019).
17. X. Shu, L. Beckmann, Y. Wang, I. Rubinoff, K. Lucy, H. Ishikawa, G. Wollstein, A. A. Fawzi, J. S. Schuman, R. V. Kuranov, and H. F. Zhang, "Designing visible-light optical coherence tomography towards clinics," *Quant. Imaging Med. Surg.* **9**(5), 769–781 (2019).
18. H.-C. Park, Y.-H. Seo, and K.-H. Jeong, "Lissajous fiber scanning for forward viewing optical endomicroscopy using asymmetric stiffness modulation," *Opt. Express* **22**(5), 5818–5825 (2014).
19. Y. Chen, Y.-J. Hong, S. Makita, and Y. Yasuno, "Three-dimensional eye motion correction by lissajous scan optical coherence tomography," *Biomed. Opt. Express* **8**(3), 1783–1802 (2017).
20. L. Huo, J. Xi, Y. Wu, and X. Li, "Forward-viewing resonant fiber-optic scanning endoscope of appropriate scanning speed for 3d oct imaging," *Opt. Express* **18**(14), 14375–14384 (2010).
21. O. M. Carrasco-Zevallos, C. Viehland, B. Keller, R. P. McNabb, A. N. Kuo, and J. A. Izatt, "Constant linear velocity spiral scanning for near video rate 4d oct ophthalmic and surgical imaging with isotropic transverse sampling," *Biomed. Opt. Express* **9**(10), 5052–5070 (2018).
22. I. A. Mahmood, S. O. R. Moheimani, and B. Bhikkaji, "A new scanning method for fast atomic force microscopy," *IEEE Trans. Nanotechnol.* **10**(2), 203–216 (2011).

23. D. Ziegler, T. R. Meyer, A. Amrein, A. L. Bertozzi, and P. D. Ashby, "Ideal scan path for high-speed atomic force microscopy," *IEEE/ASME Trans. Mechatron.* **22**(1), 381–391 (2017).
24. D. Shepard, "A two-dimensional interpolation function for irregularly-spaced data," in *Proceedings of the 1968 23rd ACM national conference*, (1968), pp. 517–524.
25. P. Ortiz, M. Draelos, R. P. McNabb, A. M. Narawane, C. Viehland, A. N. Kuo, and J. A. Izatt, "Autoaligning and autofocusing robotic optical coherence tomography of the retina for subject motion, gaze, and defocus compensation," in *Optical Coherence Tomography and Coherence Domain Optical Methods in Biomedicine XXV*, vol. 11630 (SPIE, 2021), p. 116300H.
26. P. Ortiz, M. Draelos, R. P. McNabb, A. N. Kuo, and J. Izatt, "Autofocusing and autoaligning robotic optical coherence tomography," *Investigative Ophthalmology & Visual Science* **62**(8), 2555 (2021).
27. W. T. Joines, W. D. Palmer, and J. L. T. Bernhard, *Microwave Transmission Line Circuits* (Artech House, 2013), chap. 4.3.
28. J. Bechtle and G. F. Trommer, "S-matrix representation of polarisation dependent fibre optic couplers for the simulation of optical networks," in *Proceedings of 2005 IEEE/LEOS Workshop on Fibres and Optical Passive Components, 2005.*, (IEEE, 2005), pp. 192–197.
29. J. Bushberg and J. Boone, *The Essential Physics of Medical Imaging*, Online access: Ovid Technologies LWW Doody's Core Collection 2019 (Wolters Kluwer Health, 2011).
30. B. Saleh and M. Teich, *Fundamentals of Photonics* (Wiley, 2007).
31. R. Leitgeb, C. K. Hitzenberger, and A. F. Fercher, "Performance of fourier domain vs. time domain optical coherence tomography," *Opt. Express* **11**(8), 889–894 (2003).
32. M. A. Choma, M. V. Sarunic, C. Yang, and J. A. Izatt, "Sensitivity advantage of swept source and fourier domain optical coherence tomography," *Opt. Express* **11**(18), 2183–2189 (2003).
33. E. J. Hastings, J. Mesit, and R. K. Guha, "Optimization of large-scale, real-time simulations by spatial hashing," in *Proc. 2005 Summer Computer Simulation Conference*, vol. 37 (Citeseer, 2005), pp. 9–17.
34. C. A. Schneider, W. S. Rasband, and K. W. Eliceiri, "Nih image to imagej: 25 years of image analysis," *Nat. Methods* **9**(7), 671–675 (2012).
35. U. Hassan and M. S. Anwar, "Reducing noise by repetition: introduction to signal averaging," *Eur. J. Phys.* **31**(3), 453–465 (2010).
36. J.-P. Thirion, "Image matching as a diffusion process: an analogy with maxwell's demons," *Med. Image Anal.* **2**(3), 243–260 (1998).
37. T. Vercauteren, X. Pennec, A. Perchant, and N. Ayache, "Diffeomorphic demons: Efficient non-parametric image registration," *NeuroImage* **45**(1), S61–S72 (2009).
38. F. Wei, K. Hagan, C. Y. Li, A. N. Kuo, J. A. Izatt, and A.-H. Z. Dhalla, "Spiral scanning for improved fixation in confocal scanning laser ophthalmoscopy," in *Ophthalmic Technologies XXXIII*, (SPIE, 2023), p. PC123600X.